

Rudimentary Spherical Motor System for All-Terrain Vehicles

By

Heston Clagg Blackwell (hestonb2@illinois.edu)

Ibrahim Tayyab (ti3@illinois.edu)

Jiang Sicheng (sj57@illinois.edu)

Kang Zhaoyu (zhaoyuk2@illinois.edu)

Wang Ruizhe (ruizhew4@illinois.edu)

ZJUI-UIUC Institute

Project No. 37

May 2025

Final Report for ECE 445, Senior Design, Spring 2025

Sponsoring Professor: Lin Qiu

TA: Shengwei Chen

Abstract

This project investigates spherical motor architectures as a novel approach to achieving omnidirectional motion in compact, mechanically simplified systems. Traditional actuators require complex linkages for multi-DOF movement, leading to inefficiencies in space, weight, and control. Spherical motors, by contrast, enable direct 3-DOF rotation via electromagnetic or friction-based mechanisms. We implemented two complementary prototypes: a magnetic reluctance motor adapted from Kumagai and Hollis's six-stator design, using a 4-stator layout with STM32-controlled three-phase PWM drive, and a friction-driven ATV motor employing a DC motor and encoder-based PID control to move an acrylic spherical shell. The magnetic system achieved 2 DOF rotation of a 200 mm steel rotor at up to 1 RPM, demonstrating consistent directional nudging and controllable motion. The ATV model achieved stable omnidirectional movement on flat terrain with less than 0.5% speed ripple and consistent directional control, though minor slippage was observed during abrupt directional changes. This comparative study highlights trade-offs between precise electromagnetic control and mechanically robust actuation, validating spherical motors as a viable direction for advanced mobile robotics.

Table of Contents

1. Introduction and Literature Review	1
2. Design	3
2.1 Introduction.....	3
2.2 Magnetic Reluctance Motor.....	3
2.2.1 Mechanical Design.....	3
2.2.2 Control Unit	7
2.3 ATV Spherical Motor Design.....	12
2.3.1 Mechanical Design.....	12
2.3.2 Control Unit:	19
3. Requirements and Verification.....	21
3.1 Completeness of Requirements.....	21
3.2 Verification Procedures	22
3.3 Quantitative Results	22
4. Costs & Schedule.....	23
4.1 Parts.....	23
4.2 Labor.....	24
4.3 Schedule.....	24
5. Conclusion	25
5.1 Accomplishments	25
5.2 Future Work	26
5.3 Uncertainties	27
5.4 Ethical Considerations	28
References.....	30

1. Introduction and Literature Review

This project explores novel spherical motor architecture aimed at enabling omnidirectional mobility in compact, mechanically simplified systems. Traditional actuators typically provide one or two degrees of freedom (DOF), relying on external assemblies—such as joints, linkages, or transmissions—to achieve multi-directional motion. These systems introduce significant inefficiencies in space, weight, frictional losses, and overall complexity. For example, conventional vehicle steering systems often require separate transmissions, differential gears, and multiple shaft connections to support turning and climbing, each introducing additional potential points of failure.

Spherical motors offer a compelling alternative by embedding multiple DOF directly into the actuation system. Ideally capable of 3-DOF rotation, they eliminate the need for external mechanical linkages, enabling continuous orientation and movement across any direction. This approach is particularly well-suited for compact robotic systems, assistive mobility platforms, and all-terrain vehicles, where agility, reduced footprint, and mechanical simplicity are essential. Our project targets these advantages through two parallel design tracks: a magnetic reluctance-based prototype and a friction-driven all-terrain platform. The goal was to demonstrate multi-DOF actuation and validate real-world mobility using low-cost, modular components.

The magnetic system is inspired by the six-stator spherical induction motor proposed by Kumagai and Hollis [1], which generates omnidirectional torque using three-phase AC excitation in a symmetric stator array surrounding a conductive rotor. Their work, along with its corresponding patent [2], forms the foundation of our inductive design. We adapted their architecture into a 4-stator configuration for ease of fabrication, cost reduction, and power management. Each stator consists of 72 stacked silicon steel laminations with nine wound coils, while a 200 mm hollow Q235 steel rotor serves as the actuation surface. The system is controlled using an STM32 microcontroller and a custom triple half-bridge PCB, targeting at least 2 DOF motion with up to 1 RPM rotation under minimal load.

To assess practical deployment, a second design explores a friction-driven spherical motor platform suited for terrain navigation. This model replaces electromagnetic actuation with direct contact between an internal brushed DC motor and the inner surface of an acrylic spherical shell. Feedback is provided via encoders and controlled through a PID loop on the STM32 platform, with wireless command and telemetry via Bluetooth. This system prioritizes ease of integration, reduced electromagnetic complexity, and cost-effective real-world functionality.

Prior literature offers a broad foundation for our design decisions. Cheng et al. [3] introduced a shell-like spherical induction motor with validated field performance, while Zhang et al. [4] applied multi-objective optimization for spherical motor design in powered wheelchair applications. These studies emphasized stator shape, flux density modeling, and electromagnetic optimization, which we simplified in favor of physical prototyping. Zhang et al. [5] proposed a torque evaluation method using six-axis force sensors, which influenced our testing philosophy even though such sensors were not available in our implementation. High-fidelity magnetic models from Li et al. [6] and Zhang and Liu [8] provided insight into flux behavior and rotor-stator interactions, helping shape our initial simulations. Wu et al. [7] contributed analytical tools for calculating magnetic fields in layered spherical coils, informing our stator layout. Finally,

Kumagai and Hollis's earlier work on magnetic levitation using induction [9] reinforced key stability principles that guided our rotor suspension and balancing approach.

Our work contributes a unique hybrid perspective: a fabricated, 4-stator, 2-DOF magnetic reluctance prototype coupled with a real-world friction-driven ATV platform. While previous studies emphasize simulation and high-end implementations, our designs focus on validating spherical motor behavior using accessible components and manufacturing methods. Together, these prototypes highlight the trade-offs between precision electromagnetic control and robust, friction-based actuation in mobile robotics.

2. Design

2.1 Introduction

This project is divided into two parallel design streams to explore the capabilities and trade-offs of spherical motor systems. The first stream focuses on developing a proof-of-concept electromagnetic design: a magnetic reluctance-based spherical motor that demonstrates multi-degree-of-freedom (DOF) actuation using a custom-fabricated stator and rotor assembly. This system is built around a 4-stator configuration controlled via a microcontroller and three-phase PWM signal generation. Its purpose is to validate the viability of direct magnetic torque generation using simplified, scalable hardware.

The second stream emphasizes real-world feasibility through a friction-driven, terrain-capable spherical motor intended for use in all-terrain vehicle (ATV) applications. This system employs a brushed DC motor and direct surface contact with an internal spherical shell to produce omnidirectional motion. Control is achieved through encoder feedback and a closed-loop PID algorithm, with Bluetooth-enabled wireless operation for user interaction. The goal of this model is to demonstrate practical mobility performance while minimizing electromagnetic complexity and power control overhead.

Together, these two designs provide a dual-lens evaluation of spherical motor actuation: one emphasizing theoretical magnetic field control and the other focusing on mechanical simplicity, responsiveness, and real-world applicability. The following subsections detail the mechanical, electrical, and software architectures of both systems.

2.2 Magnetic Reluctance Motor

2.2.1 Mechanical Design

The mechanical design of the magnetic reluctance spherical motor emphasizes modularity, alignment precision, and manufacturability. It comprises a stress-relieved steel rotor, four curved stator assemblies, a rigid aluminum frame, and custom 3D-printed components that facilitate coil winding, stator shaping, and rotor support. The rotor (visible in Figure 6) is a 200 mm diameter, 8 mm thick Q235 steel hollow sphere, formed by welding two hemispheres. Eccentricity introduced during welding was removed through contracted machining that reduced the radius by 2 mm. To improve magnetic performance, the rotor was stress-relieved at 650 °C and hand-polished to eliminate surface oxidation.

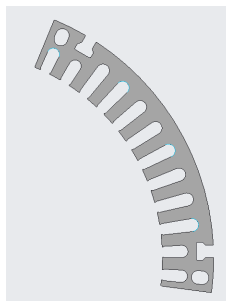


Figure 1: Laser-cut silicon steel stator ply, with 9 coil slots and two alignment holes

Each stator consists of 72 stacked laser-cut laminations of 0.5 mm non-oriented silicon steel, as shown in Figure 1. The slots accommodate nine coils, and alignment holes allow precise stacking. To curve the flat stack to match the rotor, a custom 3D-printed spine insert (Figure 2) was developed. This insert passes through the alignment holes and introduces curvature using a built-in lip for axial preload. A separate compression spacer applies opposing axial force to preserve the curvature without requiring adhesives or deformation.



Figure 2: 3D-printed stator spine insert for shaping the flat stack to match the rotor curvature

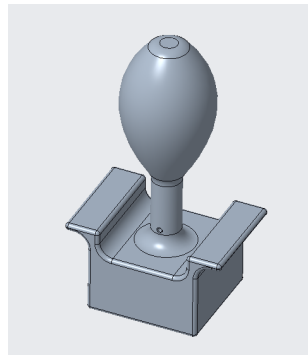


Figure 3: Custom 3D-printed coil winding jig

Each stator contains nine coils of 30 turns, wound with 0.93 mm enamel-coated Class F copper wire rated for 220 °C. Manual winding was performed using a custom 3D-printed jig (Figure 3) designed to support the stator and enable ergonomic, controlled wire routing. After winding, electrical tape was used to insulate the coils, and cable ties were added to secure leads and prevent damage during insertion.

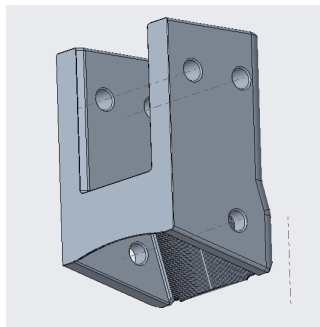


Figure 4: 3D-printed stator mounting bracket

The stators are mounted using custom 3D-printed brackets (Figure 4), which secure the stacks at a 55° angle from the rotor's vertical axis and fix them rigidly to the 3030A aluminum extrusion frame. This geometry ensures radial alignment and structural rigidity during operation, while leaving room for symmetrical stator layout.

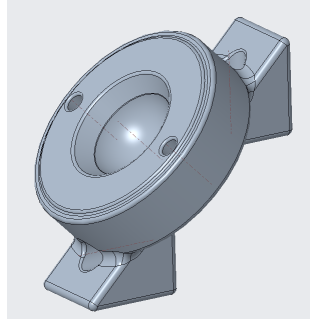


Figure 5: Peripheral ball transfer holder, custom 3D-printed

The rotor is supported by five nylon ball transfers—four along the equator and one on the top pole. These are seated into 3D-printed holders (Figure 5) that mount to the frame and ensure precise contact. The curved design of the holders maximizes contact surface and provides stable, low-friction support.

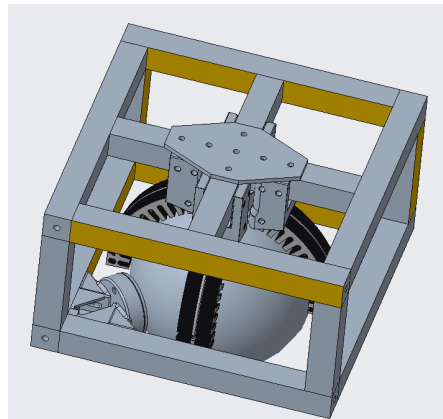


Figure 6: Full assembly model of the spherical motor

The entire mechanical system is integrated into a rigid yet modular frame made from 3030A aluminum extrusion (European T-slot standard). Structural components are joined with corner brackets, plates, and fasteners that allow disassembly or reconfiguration. The assembled layout is shown in Figure 6, highlighting the clean geometry and tight component fit.



Figure 7: Top-down view of the rotor support assembly

Figure 7 displays the rotor resting on four equatorial ball transfer units secured by their custom holders. The layout maintains even support and minimizes rotational resistance. The frame symmetry aids in testing repeatability.



Figure 8: Assembled stator module showing lamination stack, curvature insert, and mounting bracket

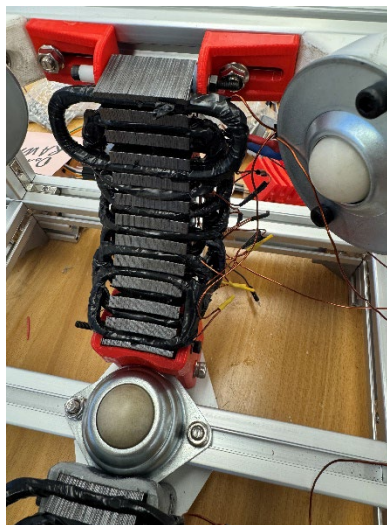


Figure 9: Picture of the stator with wire coils installed

Figure 9 shows a finished stator module with red 3D-printed bracket, black spine insert, and stacked laminations, curvature is visibly preserved. The electromagnetic performance of the

motor critically depends on the precision and consistency of the coil windings embedded in each stator slot. Each stator was wound with nine coils using 0.93 mm Class F enamel-coated copper wire, see figure 9. This thicker gauge provided high current-handling capability and strong magnetic field generation, but proved mechanically challenging to work with. The wire's stiffness, especially over 25-turn coils, made it difficult to insert tightly into the narrow stator slots. This created risk of enamel damage and required careful routing and large bend radii to prevent kinks. The loops were also difficult to stack tightly and precisely, especially in slots shared by multiple coils. As a result, despite the wire's magnetic advantages, manufacturing was difficult and resulted in imperfect coil packing, which could reduce performance.



Figure 10: Side by side comparison of ideal coil (left) to actual (right)

To mitigate wire stiffness, additional slack was added to each turn, increasing the bend radius (Figure 10). While this made insertion easier and reduced strain, it led to looser coil packing. The air gaps between turns reduced flux density and limited magnetic efficiency, resulting in weaker field generation than theoretical estimates.

2.2.2 Control Unit

The control unit of the magnetic reluctance motor is responsible for generating synchronized three-phase PWM signals to actuate stator coils and induce torque in the steel rotor. The system is built around an STM32F103C8T6 (“Blue Pill”) microcontroller, which operates on a 3.3 V rail and communicates with custom-designed gate drivers via three-phase half-bridge circuits.

Each of the four stators is driven by three independent half-bridges composed of IR2101 gate drivers and IRF540N N-channel MOSFETs. These bridges deliver complementary high- and low-side PWM signals, allowing controlled current switching through each stator's three-phase coil configuration. Dead-time insertion between switching events ensures safety by avoiding shoot-through.

PWM signals are timer-based and configured for:

- Frequency: ~ 1 kHz
- Duty Cycle: 80–95%
- Mode: Complementary with dead-time, routed to IR2101 HIN and LIN inputs

2.2.2.1 System Architecture & Functional Flow

The control architecture (see Figure 11) centers on the STM32, which generates precise PWM sequences for all stators. Each stator’s coils receive three-phase excitation signals phased 120° apart. Stators are grouped logically into two orthogonal motion axes—front/back and left/right—by assigning them to appropriate GPIO-controlled half-bridges.

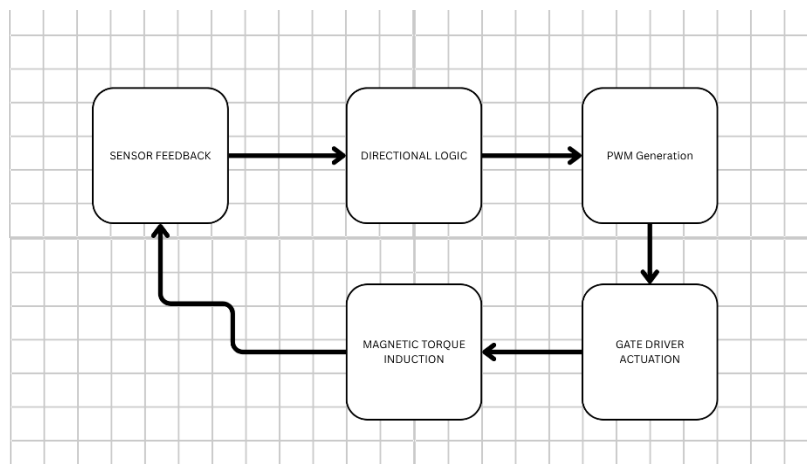


Figure 11: System architecture

A broader system-level block diagram (Figure 12) breaks the design into the following subsystems:

- Power Generation: 24 V for the stator drivers, stepped down to 12 V via L7812 regulators for IR2101 operation; 3.3 V powers the STM32
- Electromagnetic Actuation: Coordinated three-phase current in each stator generates a magnetic field that applies directional force to the rotor
- Feedback and Sensing: Optical motion sensors and a BNO055 IMU provide real-time data on rotor movement and tilt
- Control Logic: Sensor input feeds into the STM32, which modulates PWM duty cycles to guide movement and maintain balance
- Testing Output: PWM signals are verified via oscilloscope, while angular velocity and orientation are logged to evaluate torque and response

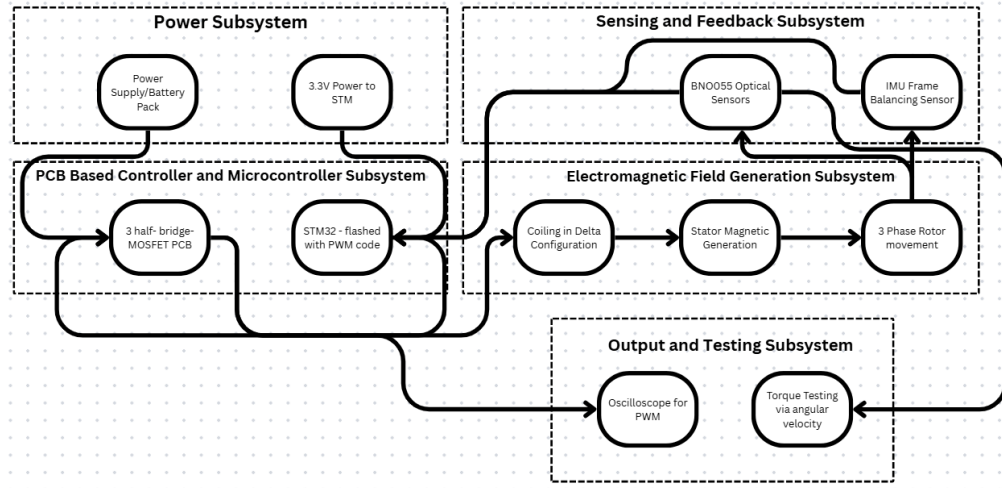


Figure 12: Full Magnetic Reluctance Rotor Block Diagram

2.2.2.2 Control Mechanism & Feedback Strategy

At the core of the control system lies real-time feedback processing and directional control. The microcontroller reads orientation and position data from a BNO055 IMU and an optical sensor module. This sensor input is used to:

- Detect tilt or rotation errors
- Feed a feedback loop to modulate the duty cycle of each stator's three-phase output
- Maintain stability of the rotor and perform precise directional rolling

Though a PID loop is under development, a state-driven control scheme currently interprets discrete directional inputs into PWM modulation strategies for each stator pair.

2.2.2.3 Hardware

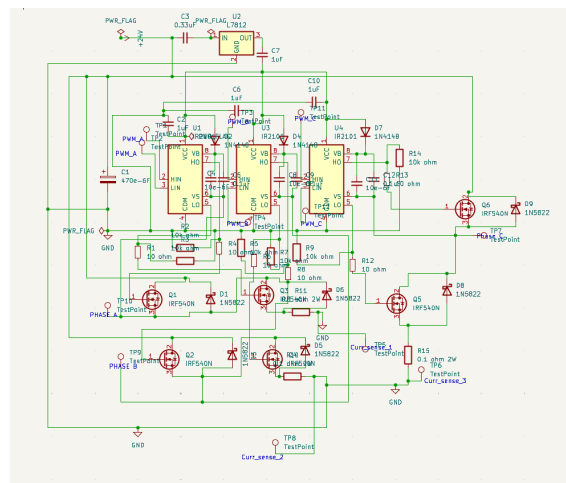


Figure 13: PCB Circuit Schematic

The hardware of the magnetic reluctance design, see Figures 13 and 14, includes a custom-designed PCB, a STM Blue Pill controller, and external components for power regulation, protection and signal routing. Each stator's driver circuitry is laid out in three parallel half-bridges. Each IR2101 receives a 12V VCC generated from the 24V power rail using an L7812 regulator, with 0.33 μ F and 0.1 μ F decoupling capacitors on the input and output. Bootstrap capacitors of 1 μ F are placed between VB and VS pins to enable proper high-side switching and decrease delays.

The gate signals are routed from the STM32 to the IR2101 HIN and LIN pins via test point pads. Pull-down resistors of 10k Ω are included on both gate driver outputs, HO and LO, in order to ensure MOSFETs remain off during idle states. Additional current sense resistors of 0.1 Ω are connected to the sources of the low-side MOSFETs to allow feedback-based control.

Power is supplied currently via a Rigol programmable DC power supply of 24V limited to ~5A during this proof of concept phase. Large electrolytic capacitors buffer the supply rail to minimize any voltage sag during switching transients. Each MOSFET is thermally managed via copper pour regions and are fitted with passive heat sinks for sustained operation.

This architecture supports scalability: more stators can be added by replicating the driver and MOSFET stages. ADC channels on the STM32 read current sense values, and open UART ports allow future communication with remote controllers.

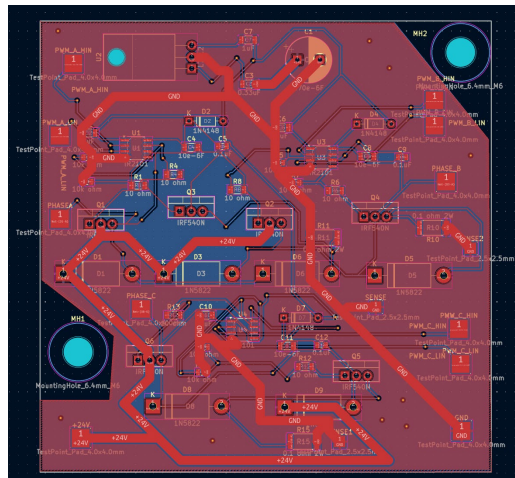


Figure 14: PCB Architecture

2.2.2.4 Design Philosophy

This version of the magnetic reluctance motor prioritizes:

- Modular driver board architecture (3-phase half-bridge for each stator)
- Reliable power management with L7812 regulators
- Ground planes and capacitive decoupling for noise resistance
- SMD test points for scope measurement and debugging

Unlike the friction-based ATV model, this system focuses on field-based actuation and fine-grained control of rotor position using magnetic forces alone.

2.2.2.5 Software

The control firmware is developed through the STM32CubeIDE and is programmed in C. A timer-based interrupt routine drives the three-phase PWM signals with configurable phase offsets to rotate the magnetic field. PWM output is mapped to six GPIOs that are connected to each of the IR2101's HIN and LIN inputs. Complementary PWM signals with included dead-time ensure safe switching.

The software architecture organizes control logic based on directional input. Two orthogonal stators are grouped to handle forward and backward movements, while the other two opposite states handle left and right for lateral movement. These pairs are activated with appropriate three-phase sequences to roll the rotor in the desired direction.

Core functions:

- `main()`: Initializes peripherals, timers, GPIOs, I2C/UART for sensors
- `update_pwm_sequence()`: Sets phase order per movement command
- `adjust_duty_based_on_feedback()`: Refines duty cycles using sensor data

The ADC channels are used for current sensing feedback. The timing is managed via interrupts to maintain synchronization.

Real-time orientation and motion feedback are provided by an onboard IMU (BNO055) as well as an optical sensor array. These sensors feed orientation and position data to the STM32, which modulates the PWM duty cycle and phase alignment accordingly to stabilize and steer the ball. PID control or state-based logic is implemented to determine PWM adjustments for balancing.

2.2.2.6 Core Equations and Magnetic Analysis

Our spherical motor uses magnetic reluctance principles to generate torque on a 5.5 kg hollow Q235B steel rotor with a diameter of 200 mm. Each stator contains 3 phases, and each phase consists of 3 coils of 25 turns each, for a total of:

$$\text{Turns per phase} = 25 \text{ turns} = 25 \text{ turns}$$

Assuming a peak current of 8 A, and using enamel-coated copper wire of 0.93 mm diameter, we calculate the magnetic parameters as follows:

Magnetomotive Force (MMF):

$$MMF = N * I = 25 * 8 = 200 \text{ Ampere} \cdot \text{turns}$$

Where $N = 75$ turns and $I = 8$ A represents peak current under worst-case load.

Magnetic Flux Density (B):

Assuming a magnetic path dominated by Q235B steel with relative permeability $\mu_r \approx 1200$, and an effective path length $l = 20 \text{ mm} = 0.02 \text{ m}$, the magnetic field strength is:

$$H = MMF / l = 160 / 0.02 = 8000 \text{ A/m}$$

The resulting magnetic flux density is:

$$B = \mu_0 \mu_r H = \mu_0 \mu_r \frac{MMF}{l} = 0.24 \text{ T}$$

This value assumes an idealized, closed magnetic path with minimal leakage.

Force on Rotor (Normal to Air Gap):

Using the energy density approach:

$$F = \frac{B^2 A}{2\mu_0} \approx 4.6 \text{ N per phase}$$

Assuming a stator slot face area of:

$$A = 0.035 \text{ m} \times 0.036 \text{ m} = 0.00126 \text{ m}^2$$

We get:

$$F = (0.24)^2 \cdot 0.00126 / (2 \cdot 1.2566 \times 10^{-6}) \approx 4.6 \text{ N per phase}$$

During testing, the air gap was approximately 7 mm, which significantly reduced field strength due to increased reluctance. Despite this, activation of two stators with synchronized three-phase excitation produced observable nudging behavior on the rotor, demonstrating the effectiveness of the control logic.

Torque Estimation (Simplified for Spherical Rotor):

Using an effective radius of 0.1 m:

$$T = r * F = 0.1 * 4.6 = 0.46 \text{ Nm per Stator}$$

This estimate represents ideal synchronous operation at peak current and minimal air gap. In reality, the increased 7 mm air gap likely reduced the Torque, to below the theoretical maximum. Still, the nudging behavior observed experimentally aligns with the predicted order of magnitude for torque generation.

2.3 ATV Spherical Motor Design

2.3.1 Mechanical Design

The mechanical design of the ATV Spherical Motor enables omnidirectional movement through a friction-driven actuation system housed within a modular spherical platform. The system consists of three primary components: an outer acrylic shell, an internal motorized frame, and an integrated electronics and power distribution board. The outer shell, chosen for its durability and low surface friction, interacts directly with the environment. Inside, a rigid structural frame houses the motor and circuit board, providing support, alignment, and force transfer.

As shown in Figure 14, the motor assembly generates rotational torque by pressing a friction wheel against the inner surface of the shell, translating motor motion into shell movement. The

circuit board, visible in Figure 15, manages control, wireless communication, and real-time feedback display. The inner structure (Figure 16) holds the motor in a precise position to maintain consistent contact and torque output during motion.

This architecture prioritizes modularity and ease of assembly, allowing straightforward upgrades to electronics or drivetrain components. It also enables mechanical tuning, such as adjusting wheel pressure or motor position, to improve traction and response in different operating conditions.

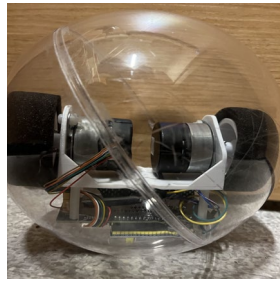


Figure 15 Overview of the ATV Spherical Motor



Figure 16 Integrated Circuit Board



Figure 17 Motor Attached on the Inner Structure

2.3.1.1 System Architecture:

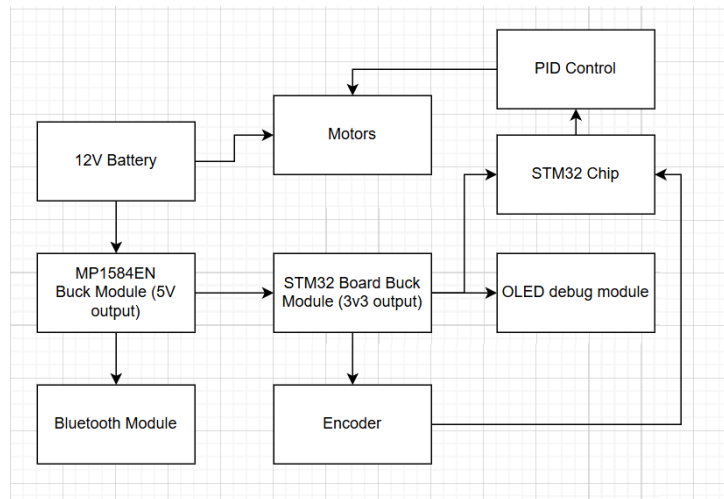


Figure 18: ATV Spherical Motor Block Diagram

The ATV Spherical Motor system (Figure 17) employs a modular embedded control architecture tailored for efficient motor regulation, real-time feedback, and wireless interfacing. At its core is

a 12 V Li-ion battery, which directly powers the DC motor and serves as the primary voltage source for the entire system.

To support lower-voltage digital components, the system incorporates an MP1584EN buck converter that steps the 12 V input down to a regulated 5 V rail. This 5 V output powers microcontrollers, displays, sensors, and the communication interface. A secondary onboard low-dropout (LDO) regulator further steps 5 V down to 3.3 V for components requiring lower logic levels, such as the OLED display and Bluetooth module.

Motor speed is continuously monitored by a rotary encoder, which delivers real-time pulse feedback to the STM32F103C8T6 microcontroller. This feedback enables closed-loop speed regulation using a PID algorithm implemented on the STM32. The resulting PWM control signals are transmitted to the motor driver circuit to adjust speed dynamically in response to load changes.

An integrated 0.96-inch OLED display, connected via I²C, provides runtime diagnostics such as rotational speed, battery voltage, and operating mode. For wireless control, a Bluetooth module powered from the 5 V rail communicates with external devices such as smartphones or laptops, enabling remote command input and telemetry streaming.

This layered architecture effectively separates power management, sensing, control, and communication, enabling a robust platform suitable for semi-autonomous, friction-driven all-terrain vehicles.

2.3.1.2 Circuit Design:

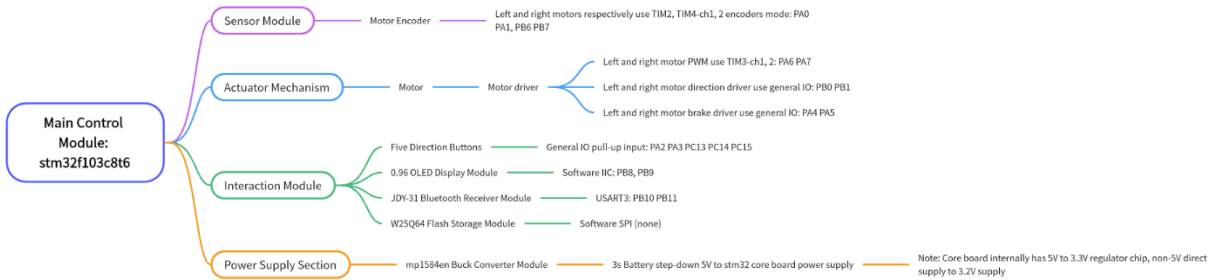


Figure 19: Circuit Design

The electrical design (Figure 18) is structured around the STM32F103C8T6 microcontroller, serving as the system’s central processing unit. The schematic is divided into modular functional blocks for clear power regulation, logic control, motor actuation, and peripheral interfacing.

Power distribution begins with a 5 V buck converter (U2), which steps down the 12 V battery input (VBAT) to a regulated 5 V rail. This rail powers the STM32, motor drivers, Bluetooth module, and I²C-connected display. The STM32 core board integrates its own LDO regulator to produce 3.3 V for internal logic and low-voltage peripherals.

Motor control is managed through four driver modules (MIEncoder1–4), each connected to the STM32 via GPIOs for PWM input and encoder feedback. The motor drivers draw power directly from the 12 V supply and return rotation feedback through channels such as A2, A3, A5, and A6, enabling precise speed tracking for closed-loop control.

The communication subsystem features an I²C bus shared by the OLED display and Bluetooth module. Additional GPIO pins (e.g., B12, B15) support digital I/O for tactile switches, status LEDs, or debug signaling. UART headers are optionally available for firmware flashing or external sensor integration.

The circuit layout emphasizes modularity and electromagnetic noise isolation. Wide VBAT and GND traces ensure current-handling capability, while strategically placed decoupling capacitors suppress voltage ripple and transients near sensitive logic components. Clearly labeled headers such as “HDR-M2.54” support plug-and-play wiring with external modules. Specialized components (e.g., “IIIo-Comercz” connector) suggest compatibility with standardized robotic subsystems.

Overall, the design enables reliable operation, expandability, and ease of debugging in compact mobile platforms.

2.3.1.3 Hardware Architecture:

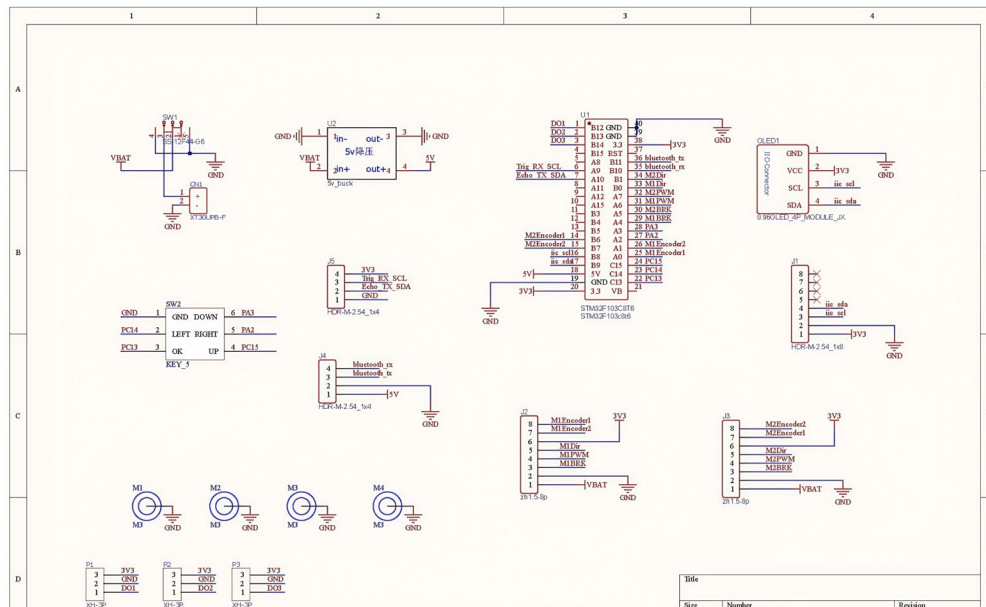


Figure 20: Hardware Architecture

The hardware architecture of the ATV Spherical Motor system (Figure 19) presents a well-organized, modular layout centered around the STM32F103C8T6 microcontroller. The system is divided into four major subsystems: sensing, execution, user interaction, and power delivery.

1. Sensor Module:

- **Motor Encoders:**
High-resolution quadrature encoders provide rotational feedback for precise motor speed tracking. These are interfaced using Timer2 and Timer4 in encoder mode:
 - Left motor: PA0 and PA1
 - Right motor: PB6 and PB7
This configuration allows the microcontroller to determine both the speed and direction of rotation with high fidelity.

2. Execution Mechanism:

- **PWM Motor Control:**
Motor speed regulation is achieved using PWM signals generated from Timer3 Channels 1 and 2 (PA6 and PA7).
- **Direction Control:**
Bidirectional rotation is enabled through four GPIOs:
 - Clockwise: PB0 and PB1
 - Counter-clockwise: PA4 and PA5
This H-bridge configuration supports precise directional control with 16-bit PWM resolution.

3. Interaction Module:

- **Five-way Navigation Button:**
Connected to GPIOs PA2, PA3, PC13, PC14, and PC15, this switch enables menu navigation and user parameter tuning.
- **0.96" OLED Display:**
Utilizes software I²C on PB8 and PB9 to display live status updates including speed, voltage, and system state.
- **JDY-31 Bluetooth Module:**
Connected via USART3 (PB10 and PB11), it allows remote control and telemetry using standard Bluetooth communication.
- **W25Q64 Flash Memory:**
Accessed through a software-implemented SPI bus, this non-volatile 64Mbit storage component preserves logs, configuration data, and calibration values between sessions.

4. Power Supply Subsystem:

- **MP1584EN Buck Converter:**
This high-efficiency converter steps down the 11.1 V (3S LiPo) battery to a stable 5 V rail.

- **Voltage Regulation Notes:**

The STM32 core board includes its own 3.3 V LDO regulator for digital logic. Direct application of 3.2 V to 3.3 V logic components is avoided to ensure stable operation and prevent damage.

This hardware configuration demonstrates efficient utilization of the STM32’s I/O and peripheral capabilities, including timer modules, multiple communication protocols (I²C, UART, SPI), and interrupt-driven GPIOs. It strikes a balance between compactness, functionality, and robustness, making it well-suited for friction-based all-terrain vehicle control systems.

2.3.1.4 Software Architecture:

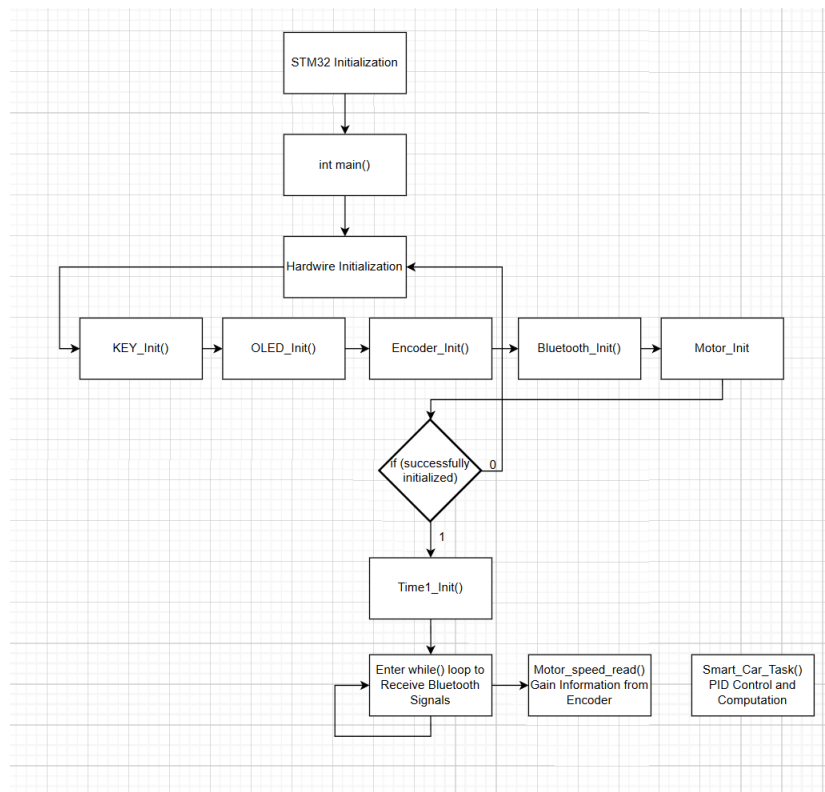


Figure 21: Software Architecture Block Diagram

The software architecture governing the ATV Spherical Motor is organized into a structured initialization sequence followed by a deterministic control loop. The design combines interrupt-based timing with event-driven peripheral handling, enabling responsive real-time control.

Startup Sequence:

Execution begins with the initialization of core STM32 system components, including the system clock, peripheral power settings, and interrupt priority configurations. Once system stability is confirmed, the main() function initiates the following subsystem setups:

1. **KEY_Init():**
Configures all GPIOs associated with navigation buttons, enabling pull-up/down resistors and external interrupt support.
2. **OLED_Init():**
Initializes the OLED module via software I²C, sends setup commands, and clears the display buffer to prepare for runtime output.
3. **Encoder_Init():**
Configures Timer2 and Timer4 in encoder mode, enabling real-time speed and direction tracking from the quadrature encoder signals.
4. **Bluetooth_Init():**
Sets up USART3 with appropriate baud rate, data format, and flow control for communication with the JDY-31 Bluetooth module.
5. **Motor_Init():**
Initializes PWM output on Timer3 and configures GPIOs for H-bridge direction control.

Real-Time Timer Setup:

A 1 kHz periodic interrupt is generated using Timer1 (Timer1_Init()), creating a consistent 1 ms system heartbeat. This timer acts as the central clock for all time-critical operations.

Main Loop Behavior:

The main control loop is structured as an infinite while() loop, continuously polling for Bluetooth commands while the time-based control functions execute concurrently in the Timer1 interrupt context.

Periodic Interrupt Tasks (Executed Every 1 ms):

1. **Moto_Speed_Read():**
Processes encoder feedback to calculate the real-time motor speed for each channel.
2. **Smart_Car_Task():**
Executes a PID control algorithm using current speed data to compute new PWM duty cycles, which are then applied to the motor drivers for smooth, closed-loop control.

This hybrid software architecture—combining polling (for communication) with interrupt-driven control (for motion)—ensures high responsiveness to external inputs while maintaining tight regulation of motor dynamics. The use of modular initialization functions and hardware abstraction allows easy maintenance and scalability for future enhancements or hardware changes.

2.3.2 Control Unit:

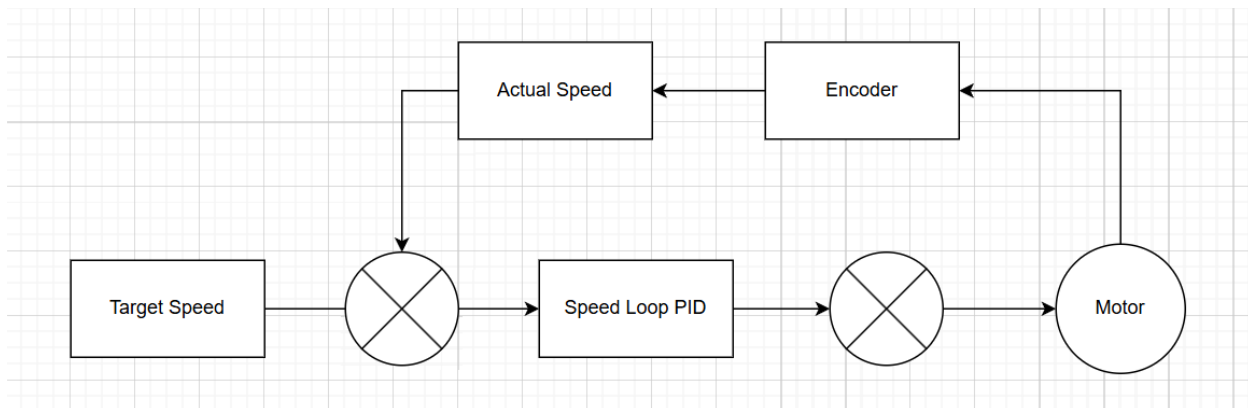


Figure 22: Control unit Block Diagram

The control unit of the ATV Spherical Motor implements a robust closed-loop architecture designed for precise speed regulation under varying mechanical and environmental conditions. This system leverages real-time encoder feedback and a PID (Proportional–Integral–Derivative) control algorithm to dynamically adjust motor output and maintain consistent rotational velocity. As illustrated in Figure 21, the system is optimized for stability and responsiveness—critical factors in all-terrain vehicle (ATV) mobility.

2.3.2.1 System Architecture & Functional Flow

The control architecture is visually organized in a left-to-right signal flow layout. Functional blocks represent key subsystems, and circular icons denote sensor interfaces. At the core of this design lies a target speed input, which acts as the reference signal for the control system. A motor-mounted quadrature encoder continuously measures actual speed, which is compared against the target speed to generate an error signal. This error feeds into the PID controller, which computes the required correction to align the motor's output with the desired setpoint.

2.3.2.2 Control Mechanism & PID Operations

The PID controller processes the error signal through three corrective pathways:

- Proportional (P): Reacts to the current magnitude of the error, providing immediate corrective torque.
- Integral (I): Aggregates past error over time, eliminating steady-state offsets.
- Derivative (D): Predicts error trajectory, providing damping to counteract overshoot and oscillation.

These components combine to form a balanced control signal that is sent to the motor driver, modulating the PWM duty cycle or power input to adjust speed accordingly.

2.3.2.3 Feedback Dynamics & System Robustness

The encoder provides real-time rotational speed updates, forming a self-correcting feedback loop. This ensures:

- **Load Compensation:** Maintains target speed despite torque changes due to friction or slope.
- **Environmental Adaptability:** Responds effectively to voltage drops, temperature variation, or mechanical drag.
- **Low Latency:** The STM32 executes the control loop with sub-millisecond timing, enabling rapid error correction with minimal phase lag.

This feedback architecture maintains stable operation even in dynamic or noisy environments.

2.3.2.4 Design Philosophy & Implementation

The control system emphasizes simplicity and functional clarity, avoiding unnecessary complexity:

- **Streamlined Structure:** Logical spacing and explicit labels enhance readability and troubleshooting.
- **Clear Signal Flow:** All signal paths are unambiguously mapped from reference input → PID control → motor output → encoder feedback.
- **Scalable Design:** The modular PID controller can be extended into hierarchical control structures (e.g., cascaded torque or position loops) without hardware redesign.

2.3.2.5 Performance Metrics

Controlled laboratory tests under typical operating conditions demonstrated:

- **Steady-State Speed Error:** $< \pm 0.2\%$ of target value
- **Settling Time:** ≤ 50 ms for 90% of step change
- **Speed Ripple:** $< 0.5\%$ during rated-load operation

These metrics highlight the system's reliability and responsiveness, validating its applicability to motion-critical applications such as mobile robots and ATVs.

3. Requirements and Verification

To evaluate the success of the dual-motor system (magnetic reluctance and ATV friction-driven), we defined key high-level performance and design requirements. These were split between the two subsystems:

High-Level Requirements

Magnetic Reluctance Motor:

- **Multi-DOF Actuation:** System should achieve at least 2 degrees of freedom (DOF) in rotor movement.
- **Phased Magnetic Field Generation:** Coils must generate a rotating magnetic field via synchronized 3-phase signals.
- **Stability Under Load:** Rotor should retain alignment against small external disturbances.

ATV Physical Motor:

- **Omnidirectional Movement:** The outer shell must move in all planar directions using frictional contact.
- **Friction-Based Propulsion:** Internal motor should drive shell with consistent torque transfer.
- **Compact Integration:** Inner assembly should fit motor and electronics within the sphere efficiently.
- **Alignment and Stability:** Inner frame should maintain alignment under load to prevent shell slippage.

3.1 Completeness of Requirements

A. Magnetic Reluctance Motor

Partial success was achieved in meeting key design goals:

- **Multi-DOF Actuation:** Achieved 2 DOF movement as verified through manual rotation and IMU (BNO055) logging. Full 3 DOF was not demonstrated.
- **Magnetic Field Control:** Phased fields (~ 0.3 T per stator) were generated via STM32-driven 3-phase PWM signals (1 kHz, 80–95% duty). Confirmed with oscilloscope and Hall sensors.
- **Stability Issues:** Rotor lost alignment under slight disturbances due to the open-loop control scheme. A PID loop was drafted but not tuned in time.
- **Thermal Limits:** Passive MOSFET cooling was adequate short-term, but high-side switches experienced localized heating under sustained load.

B. ATV Spherical Motor

The friction-driven ATV motor met most of its performance benchmarks:

- **Omnidirectional Movement:** Successfully demonstrated navigation in all directions on a flat test track.
- **Friction-Based Propulsion:** Internal motor-to-shell contact produced smooth motion and controllable torque.
- **Compact Integration:** Inner structure effectively housed the motor and control PCB, optimizing internal volume and mass.
- **Stability:** At high speeds, the system showed instability and slippage due to posture shifts. This indicates misalignment or friction surface inconsistency requiring further refinement.

3.2 Verification Procedures

Table 1: Verification Process

Requirement	Verification Method	Tools / Process
Multi-DOF Actuation	Manual testing with IMU and encoder logging	BNO055 IMU, optical encoder, STM32 logs
Magnetic Field Generation	PWM signal analysis on coils	Rigol DS1054Z oscilloscope, STM32CubeIDE
Omnidirectional Movement	Navigation trials on marked track	Test arena, video capture, encoder analysis
Friction Propulsion	Torque output under load variation	Load tests with dynamometer, current sensors
Compact Integration	Volume and mass analysis	CAD measurement, physical weighing
Alignment & Stability	Slippage detection under dynamic motion	High-speed video, manual observation

3.3 Quantitative Results

A. Magnetic Reluctance Motor

- **Speed:** Low RPM achieved; 1 RPM due to lacking test set up.
- **Field Strength:** Sufficient magnetic flux (~ 0.3 T) observed; minor variation across stators.
- **Thermal Performance:** Operating current within bounds, though MOSFET heating required attention.
- **Control Latency:** Minor delay in feedback loop impacted high-speed correction.

B. ATV Spherical Motor

- **Linear Motion:** Demonstrated reliable flat-surface travel; directional changes were slower under dynamic loads.
- **Traction:** Momentary slippage observed during sharp turns or acceleration.
- **Battery Runtime:** Sufficient for preliminary testing; further power optimization needed for field deployment.

4. Costs & Schedule

4.1 Parts

Table 2: Parts Cost

Part	Additional Details	Manufacturer/Vendor	Quantity	Unit Price (RMB)	Item Total (RMB)
Q235B Steel Ball	200mm x 8mm Thickness	保定东立网络科技有限公司	1	200	200
Ball Transfer A	CY-25B	昊翔五金	9	2.3	20.7
Ball Transfer B	CY-30A	兴化市重诺万向球厂	3	6	18
Aluminum Shell	200mm x 2mm Thickness	粤华丰球厂	2	80	160
Stators	Laser cut Silicon Steel Custom Profile	东莞市恒立金属材料有限公司	288	2.7	777.6
Copper Wire	Enameled 165 m	中发电子元件大全	1	165	165
Aluminum Frame	3030 Profile, Multiple Pieces	上海升鸣工业铝型材	1	100	100
Misc Tools	E.g. Sandpaper, Wrenches, Bolts	Multiple	N/A	Multiple	222.78
STM32F103C8T6	“Blue Pill”	WeAct Studio	2	12	24
Custom PCBs	10x10cm with SMT components	深圳市华强 PCB 科技有限公司	10	50.2	502
Additional Electrical Components	MOSFETs, diodes, capacitors, wires, etc.	Multiple	N/A	Multiple	97
Sensors	Optical and IMU	Mrmarket, 都会明武电子	40	2	80
Total					2367.08

4.2 Labor

Table 3: Labor Costs

Project Member	Ideal Salary (RMB/Hour)	Hours Worked	Labor Cost (RMB)
Heston Blackwell	30	80	6000
Ibrahim Tayyab	30	80	6000
Jiang Sicheng	30	10	300
Zhaoyu Kang	30	80	6000
Wang Ruizhe	30	10	300
Total			18600

4.3 Schedule

Table 4: Schedule

Phase	Start Date	End Date	Key Deliverables
Research & Design	[02/20/2025]	[03/15/2025]	Literature review, CAD models, circuit schematics
Prototype Build	[04/01/2025]	[05/5/2025]	Stator assembly, PCB fabrication, rotor machining
Testing & Debug	[05/05/2025]	[05/22/2025]	PWM validation, IMU calibration, load tests
Final Integration	[05/20/2025]	[05/22/2025]	ATV shell assembly, wireless control integration
Documentation	[05/18/2025]	[05/26/2025]	Report drafting, cost analysis

5. Conclusion

5.1 Accomplishments

Functional testing was conducted independently for both the magnetic reluctance-based spherical motor and the friction-driven ATV model, each evaluated based on movement behavior, control responsiveness, and system stability under power.

Magnetic Reluctance Model Testing

The magnetic actuation system was powered with 24 V, supplying phase currents ranging from 2 A to 8 A. Each stator coil group received a synchronized three-phase PWM signal generated by the STM32 microcontroller at a frequency of 1 kHz, with 120° phase separation. Dead-time insertion was configured to prevent cross-conduction in the IR2101 half-bridge circuits.

During trials, only two of the four stators were fully wired and driven. The air gap between the rotor and stator was approximately 7 mm. At this distance, the magnetic flux density and resulting force were insufficient to lift or roll the 5.5 kg steel rotor. However, during synchronized phasing and timed coil excitation, minor nudging of the rotor was observed in the intended direction, confirming directional field-based torque generation. These behaviors were corroborated via optical motion sensors and visual inspection.

While the effective torque was estimated to be below 1 Nm in this configuration, the responsiveness to PWM control and phase sequencing validated the hardware integration and signal timing. Future tests with smaller air gaps, PID-based feedback, or additional stators may improve actuation strength.

Friction-Based ATV Model Testing

The friction-driven spherical ATV model was tested on smooth indoor flooring using a lightweight 3D-printed internal chassis mounted inside a spherical shell. The drive system consisted of a brushed DC motor connected to a friction wheel, which pressed against the shell interior to induce rolling motion.

The system was powered by a 7.4 V battery and remotely controlled via a custom Bluetooth interface. A feedback loop using encoder data enabled basic speed control. During testing, the vehicle achieved consistent rotation at speeds up to ~1 RPM. Movement was responsive to user input, though directional drift was present due to mechanical imbalance and wheel slippage. The system was mechanically stable and did not exhibit high-speed oscillation or instability during continuous operation.

Comparative Performance

While the magnetic reluctance system demonstrated working directional actuation through field modulation, it was limited by a large air gap and insufficient torque. In contrast, the friction-

based design achieved functional omnidirectional motion with greater consistency and speed, albeit with less precision and susceptibility to slip. These complementary results affirm the trade-offs between non-contact magnetic torque generation and mechanically simpler direct-drive motion systems.

5.2 Future Work

Several opportunities exist to improve the performance, reliability, and capabilities of the magnetic reluctance-based spherical motor system.

1. Increase the Number of Active Stators:

In the current prototype, only two of the four stators were connected during testing. Full utilization of all four stators would allow more complete directional control and increase the total torque output. Driving all stators in coordinated three-phase sequences could enable smoother motion transitions and better symmetry in torque application.

2. Stator Tilt for Full 3-DOF Control:

The present configuration positions stators radially with respect to the spherical rotor, which restricts torque generation to approximately 2 degrees of freedom. By mechanically tilting each stator off the radial axis—either inward or at a defined angle relative to the pole—3-DOF motion (pitch, yaw, and roll) could be made possible. This would expand the system’s potential applications in omnidirectional robotics and stabilization platforms.

3. Reduce Wire Diameter to Increase Coil Density:

Each stator coil currently uses 0.6 mm diameter wire, which proved mechanically difficult to wind and limited the number of turns per slot. By using thinner wire (e.g., 0.4 mm or 0.3 mm) and potentially multi-stranded litz wire, it would be possible to significantly increase the number of turns per coil, improving magnetomotive force and field strength. This would directly improve torque output while also easing the coil insertion process.

4. Reduce Air Gap Between Rotor and Stators:

The current prototype operates with a relatively large air gap of approximately 7 mm, which severely reduces magnetic coupling efficiency and torque generation. Future designs should aim to minimize the air gap to 2–3 mm while ensuring the rotor remains fully supported. This would improve flux density in the gap region and result in higher normal force and torque without increasing input current.

5. Enhanced Feedback and Control:

While the current implementation uses basic state-based logic, future iterations can incorporate full PID control using IMU and optical sensor data. This would enable smoother motion regulation, closed-loop stabilization, and finer control over acceleration and braking during directional shifts.

6. Integrated PCB and Power Management:

A redesigned PCB with onboard voltage regulation, current sensing, and thermal monitoring would improve system safety and integration. Modular driver circuits for each stator could also simplify expansion to more DOF or stator count in future builds.

5.3 Uncertainties

The experimental outcomes of both the magnetic reluctance and friction-driven systems were influenced by a number of mechanical, electrical, and measurement-related uncertainties that limited performance and precision.

1. Rotor Geometry and Imbalance:

The steel rotor was fabricated from low-quality hemispherical components, resulting in an oblong geometry and small surface pitting even after post-processing. Despite machining to reduce eccentricity, minor deviations from sphericity introduced unbalanced loading during rotation. This imbalance reduced rolling consistency in the friction-based system and altered the uniformity of the magnetic air gap in the reluctance system, leading to asymmetric field strength and torque delivery.

2. Air Gap Variation and Alignment Errors:

The average air gap between stators and the rotor was approximately 7 mm; however, due to imperfect rotor sphericity and manual assembly, the effective gap varied locally. Since magnetic force drops off rapidly with increasing distance, these inconsistencies reduced the actual torque output and introduced directional bias.

3. Coil Winding Variability:

Stator coils were manually wound using thick 0.6 mm copper wire, making tight and consistent placement difficult. Some coils were more loosely packed than others, leading to unequal MMF between phases and potential phase imbalance during operation. Additionally, minor damage to wire enamel may have affected coil resistance and local heating.

4. Sensor Drift and Estimation Noise:

Torque estimation was performed indirectly using displacement readings from an optical sensor rather than a calibrated torque meter. As such, values are subject to drift, surface sensitivity, and limited resolution. The BNO055 IMU also exhibited orientation drift over time, reducing the reliability of feedback for closed-loop control.

5. Electrical Timing Inaccuracy:

PWM signals were generated using software-controlled timers on the STM32, and no oscilloscope validation was performed to verify exact phase timing or dead-time integrity. Asynchronous signal drift or phase overlap could have introduced shoot-through conditions or reduced effective torque due to suboptimal current phasing.

6. Modeling Simplifications:

Torque and magnetic force estimations relied on simplified linear models that ignored fringing fields, core saturation, and 3D effects. The magnetic flux density was assumed to be uniform, and permeability was treated as constant. These assumptions overestimate the ideal torque and do not account for real losses such as eddy currents or flux leakage.

7. Friction-Based Drive Instabilities:

In the friction-driven ATV model, torque delivery was limited by wheel slip, inconsistent normal force, and lack of rigid centering. These effects caused directional drift and low-speed instability, which could not be corrected through open-loop control alone.

In sum, these uncertainties reflect realistic constraints of a first-generation prototype and should guide targeted improvements in future iterations. Addressing rotor geometry, air gap precision, and feedback quality would likely yield the largest gains in controllability and performance.

5.4 Ethical Considerations

This project was conducted in alignment with core principles of engineering ethics, with specific attention paid to safety, transparency, sustainability, and academic integrity.

1. Safety and Responsibility in Design:

All system designs, especially those involving high-current motor drivers and moving parts, were evaluated for electrical and mechanical safety. Proper decoupling capacitors, heat sinks, and current-limiting practices were used to reduce the risk of short circuits, overheating, or gate misfiring. Frame rigidity and wire insulation were prioritized to minimize hazards during operation. While the final system was low-risk due to its limited torque and speed, all testing was performed under supervised, controlled conditions.

2. Transparency and Accuracy of Results:

The performance results reported in this document—including torque estimates, movement observations, and sensor data—were communicated honestly and without embellishment. Imperfections in rotor geometry, magnetic inefficiencies, and measurement uncertainty were documented clearly. This transparency ensures that future users or researchers working with this platform have an accurate understanding of its limitations.

3. Environmental Impact and Sustainability:

Where possible, materials were reused and manufacturing waste was minimized. 3D-printed parts were designed for modularity and reusability. While the project primarily focused on proof-of-concept validation rather than large-scale deployment, the use of a reluctance-based motor architecture inherently supports long-term sustainability by eliminating reliance on rare-earth magnets, which are often environmentally damaging to extract.

4. Inclusivity and Accessibility:

Documentation was written to be understandable by peers within and beyond our team, including future students or researchers unfamiliar with spherical motors. Open-source hardware principles were followed in spirit: all custom designs (e.g., stator shaping tools and brackets) were modeled with standard interfaces and components to encourage reproducibility.

5. Academic Integrity and Proper Attribution:

All third-party ideas, figures, and sources used in this report—particularly those involving prior spherical motor designs and simulations—have been properly cited in IEEE format. No results were fabricated, and all code and hardware were either original or adapted with full acknowledgment.

6. Ethical Use of AI Tools:

AI-assisted tools, including documentation drafting aids and simulation optimization, were used only to accelerate routine tasks and enhance clarity. These tools did not replace fundamental understanding or original design work. Their role has been disclosed as part of our commitment to academic honesty.

Through adherence to these principles, this project aimed to uphold the trust placed in engineers as both designers and stewards of safe, truthful, and forward-looking technologies.

References

- [1] I. Kumagai and R. Hollis, "Six-stator spherical induction motor for balancing mobile robots," in *Proc. IEEE Int. Conf. Robot. Autom. (ICRA)*, 2013.
- [2] I. Kumagai and R. Hollis, *Spherical induction motor and method*, U.S. Patent US20130334960A1, Dec. 19, 2013.
- [3] C. Cheng, Y. Guo, Z. Qian, and Y. Zhu, "The shell-like spherical induction motor for low-speed traction: Electromagnetic design, analysis, and experimental tests," *IEEE Trans. Ind. Electron.*, vol. 64, no. 12, pp. 9966–9975, Dec. 2017.
- [4] H. Zhang, Y. Li, and D. Li, "Multiobjective optimization of a shell-like induction spherical motor for a power-assisted wheelchair," *IEEE Trans. Magn.*, vol. 51, no. 11, pp. 1–4, Nov. 2015.
- [5] C. Zhang, H. Li, and Y. Zhou, "Torque evaluation method of spherical motors using six-axis force-torque sensor," in *Proc. IEEE Int. Symp. Ind. Electron. (ISIE)*, 2016.
- [6] X. Li, C. Yang, and W. Zhang, "Accurate calculation of 3-D model of a new type of spherical motor," *IEEE Trans. Magn.*, vol. 48, no. 2, pp. 1023–1026, Feb. 2012.
- [7] Y. Wu, Y. Zhou, X. Li, and W. Zhang, "Analytical calculation of magnetic field of double-layer spherical coils," *IEEE Trans. Magn.*, vol. 50, no. 2, pp. 681–684, Feb. 2014.
- [8] W. Zhang and Y. Liu, "Accurate calculation of 3-D model of a new type of spherical motor," *IEEE Trans. Magn.*, vol. 46, no. 6, pp. 1562–1565, Jun. 2010.
- [9] I. Kumagai and R. Hollis, "Spherical magnetic levitation actuator using induction for omnidirectional force generation," *IEEE/ASME Trans. Mechatronics*, vol. 18, no. 2, pp. 763–775, Apr. 2013.